ELSEVIER

Marine Geology 164 (2000) 37–51

MARINE GEOLOGY
INTERNATIONAL JOURNAL OF MARINE GEOLOGY, GEOCHEMISTRY AND GEOPHYSICS

www.elsevier.nl/locate/margeo

Comparison of measured and BSR-derived heat flow values, Makran accretionary prism, Pakistan

N. Kaul*, A. Rosenberger, H. Villinger

FB Geowissenschaften, Universität Bremen, Postfach 330 440, D-28334 Bremen, Germany

Received 29 April 1999; received in revised form 29 July 1999; accepted 2 August 1999

Abstract

During the German research cruise SO-124 on RV *Sonne* (fall 1997) on the Makran accretionary wedge off Pakistan, geophysical investigations were carried out to study the thermal regime at a gas hydrate bearing sediment in a tectonically deformed accretionary wedge. On a transect perpendicular to the strike of the deformation front 42 heat flow measurements were carried out, accompanied by seismic reflection experiments. The investigations start in the south in the abyssal plain and cover the continental slope up to 2300 m water depth.

The aim of this study is to compare the BSR derived heat flow (denoted as estimated heat flow) with the values from measurements at the seafloor. This requires the calculation of sediment physical properties at depth using empirical relationships between velocity and porosity. The value measured and corrected for sedimentation of 47 mW/m^2 south of the deformation front is slightly higher than values reported by Hutchison et al. (Earth Planetary Sci. Lett. 56 (1981) 252–262). In all basins the estimated heatflow is significantly higher than the measured values. As a result, temperatures at the BSR extrapolated from seafloor measurements are 5–6 K lower than those taken from Gas hydrate stability considerations.

As an overall trend the estimated as well as the measured heat flow show a small decrease from the deformation front to the northward thickening prism. A similar observation was made at other accretionary wedges and described by Wang et al. (J. Geophys. Res. 98 (B3) (1993) 4121–4142) and Ferguson et al. (J. Geophys. Res. 98 (B6) (1993) 9975–9984). Within the slope basins heat flow values show little variation, indicating predominantly conductive heat transport. Fluid flow might occur at the bounding faults where we have little control.

The effect of rapid sedimentation on the dynamic behavior of the BSR might also have a significant influence on the estimated heat flow values. Our data set shows clearly that detailed seismic surveys and good control of the subsurface velocity are absolute necessities for the comparison of measured and BSR-derived heat flow values. However, the uncertainty of the velocity–porosity relationship together with a high and only approximately established sedimentation rate represent crucial but missing constraints which can be gained only by drilling.

Keywords: Bottom simulating reflector; Heat flow; Sedimentation

1. Introduction

The marine part of the accretionary wedge of Makran in the Gulf of Oman, south of Pakistan (see Fig. 1), is well known for its wide spread occurence of gas hydrates, indicated by a prominent bottom simulating reflector (BSR), detectable in reflection seismic data from about 500 m water depth down to about 3300 m south of the deformation front. The Makran margin has been a target of several seismic investigations (White and Louden, 1982; Minshull and White, 1989; Minshull et al., 1992) and heat flow

* Corresponding author.

0025-3227/00/$ - see front matter
PII: S0025-3227(99)00125-5

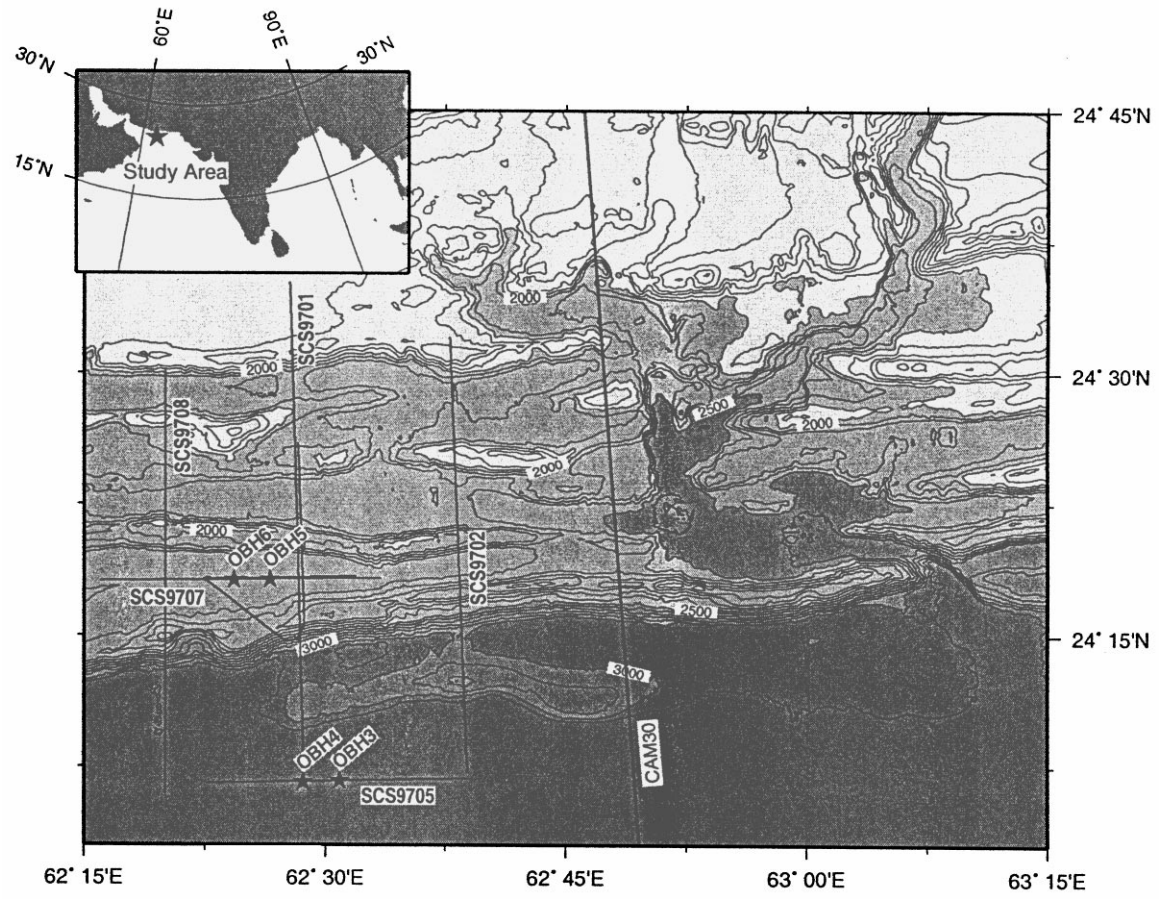

Fig. 1. Working area of research cruise SO124. The bathymetric coverage is a compilation of several actual research cruises to the Makran area, compiled by Kukowski et al. (1999). The line east of survey area represents the location of the CAM30 multichannel seismic line, published by Minshull and White (1989). Seismic velocity determinations were carried out on the southern most east–west trending line (OBH4 on line SCS9706 3) and on a midslope line (OBH6 on SCS9704) in a slope basin (see Grevemeyer et al., 2000).

measurements (Hutchison et al., 1981) in the 1980s by the geophysics group of the Cambridge University (UK). In 1997 and 1998, several research cruises with the German RV *Sonne* (legs SO122, SO123, SO124 and SO130) concentrated on detailed geophysical and geological investigations in a transect across the western part of the Makran accretionary prism off Pakistan. Extensive reflection (SO122) (Roeser and Scientific Party SO122, 1999) and refraction seismic work (SO123) (Flueh et al., 1997; Grevemeyer et al., 2000) as well as an almost complete bathymetric survey (SO123) (Flueh et al., 1997) give us a very detailed picture of the tectonics, the deep structure of the wedge and the deformation processes involved. Geological sampling during SO130 (von Rad, 1999) is completing the joint efforts to understand and quantify the tectonics and dewatering processes of this part of the accretionary prism.

In this paper we present the results from heat flow measurements obtained during the SO124 cruise in fall 1997 which concentrated on detailed geophysical investigations along a profile across the lower part of the Makran accretionary wedge. The goal of this short leg was to study the thermal regime above the BSR with heat flow measurements and a seismic depth survey.

Measured seafloor heat flow allows the calculation of temperatures at BSR if (1) the velocity structure for

depth calculation is known, (2) thermal conductivity in the subsurface is known, and (3) a purely conductive regime is assumed, i.e. advective heat transport can be neglected (Yamano et al., 1982). The thermal conductivity structure can be calculated from velocity–depth profiles through empirical relationships between velocity and porosity on the one hand and thermal conductivity and porosity on the other. The temperature at the base of the gas hydrate stability zone (GHSZ) is estimated from stability temperature and pressure conditions (Sloan, 1990; Dickens and Quinby-Hunt, 1994), using the seismically determined depth of the BSR. A comparison of BSR-derived and measured heat flow may give indications for the magnitude of the advective heat transport component, i.e. dewatering processes of the accreted sediments as modelled by Wang et al. (1993) for Northern Cascadia Margin and found by Ferguson and Westbrook (1993) at some faults at Barbados Ridge. Heat flow measurements carried out in the Makran area in the past (Hutchison et al., 1981) will not help to answer the questions related to fluid migration as they were all intentionally positioned south of the deformation front to be unaffected by fluid expulsion effects.

2. Geological setting

The accretionary complex of Makran (Pakistan; see Fig. 1) is one of the largest accretionary prisms worldwide. The oceanic crust of the Arabian Plate is being subducted at a rate of about 40 mm/a under the Eurasian Plate in NNE direction (Minshull et al., 1992). Due to the large terrigeneous input from river Indus and seasonally high biological production caused by upwelling, the sedimentation rate is extremely high with values in a range from 0.25 to 0.4 mm/a (Hutchison et al., 1981; Prins et al., 1999) (von Rad, personal communication, 1999). The resulting sediment pile reaches a thickness of 7 km. These sediments are scraped off the subducting plate to form the Makran continental margin of Iran and Pakistan (White and Klitgord, 1976; White, 1981; White and Louden, 1982). The age of the oceanic crust underlying the wedge cannot be determined using magnetic seafloor spreading anomalies due to their virtual absence. Hutchison et al. (1981) estimate an age of 70–100 Ma by using the measured mean heat flow value of 43 mW/m^2, corrected for sedimentation in conjunction with the plate cooling model (Parsons and Sclater, 1977).

On single channel seismic line SCS9701 (for details see Section 3) the main features of the compression process can be observed (Fig. 2; location of profile see Fig. 3). The seismic profile shows the start of the deformation front at about shotpoint 1900 in the south. After the first bulge seafloor rises steeply from the abyssal plain to the first ridge. Between the anticlinal ridges are sedimentary basins with northerly dipping reflectors and increased dip with depth, indicating synsedimentary uplift. Underneath the ridges no continuous reflectors can be observed, most likely a result of the deformation process. A BSR is clearly visible at about 0.6 s TWT (two-way-travel time) below the seafloor at the northern end of the profile. The thickness of the section above the BSR increases as the water depth—and hence pressure—increases to the south. It is present south of the deformation front (0.75 s TWT at shotpoint 1900), although difficult to identify as it is parallel to seismic reflectors. A detailed discussion of the seismic signature of the BSR can be found in Grevemeyer et al. (2000).

3. Geophysical measurements

3.1. Seismic measurements during SO124

All heat flow sites were located about 80 km south of the Pakistan coast on a north–south profile perpendicular to the general strike of the main structures, extending from the deformation front across four slope basins. Three single channel seismic lines were acquired (Fig. 3) to map local sedimentary structures and the depth of the BSR along strike.

Three west–east oriented cross-lines along a sedimented basin and seaward of the deformation front connect all lines. A single small GI-gun (TM of SSI) was used, operated in harmonic mode. The chamber volume of 1.23 + 1.23 l yielded enough energy to penetrate the sediments down to about 1.0 s TWT below seafloor. The result is a virtually bubble free seismic section beyond the depth of the BSR with good resolution vertically (30–80 Hz signal frequency) and horizontally (25 m

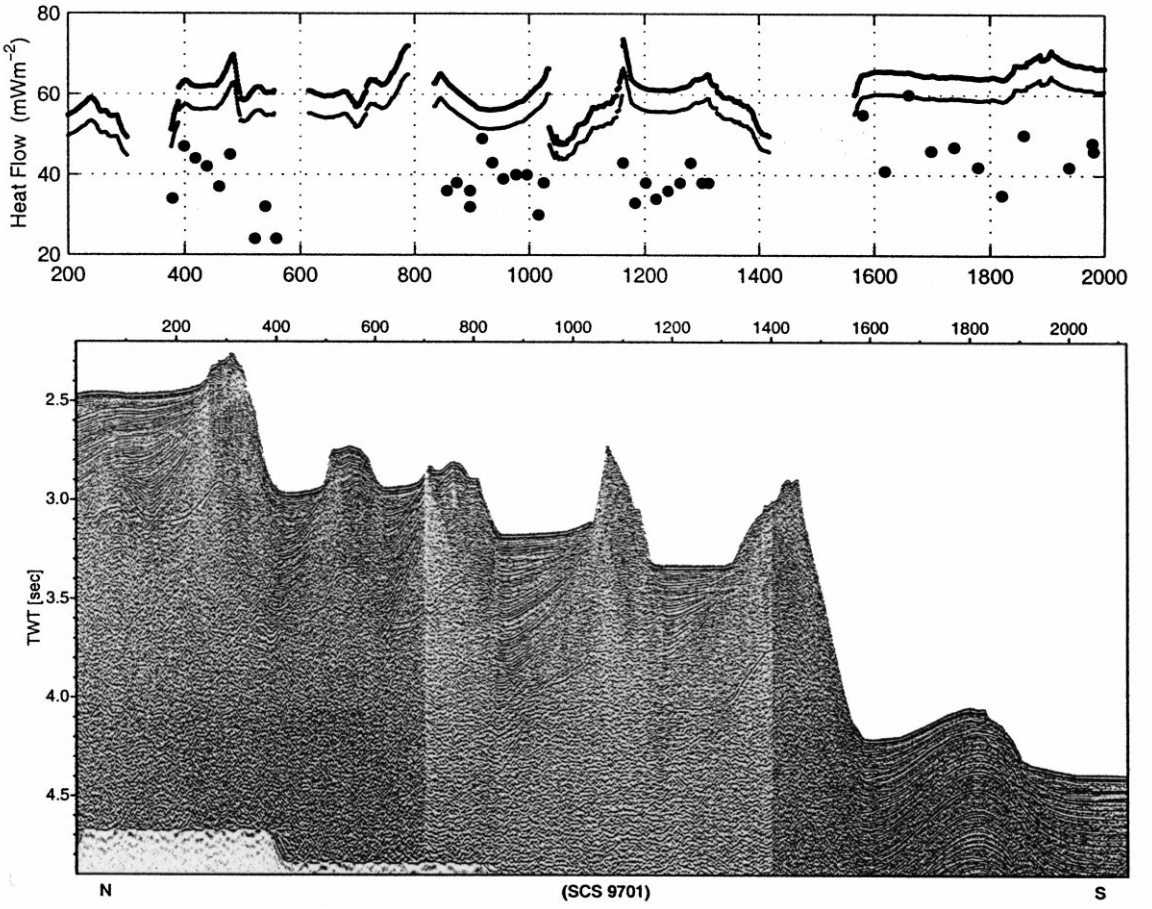

Fig. 2. Measured and estimated heat flow (top) and time migrated seismic section (bottom). Seismic line SCS9701 in the center of the survey area is the base for subsequent positioning of heat flow measurements (top, solid circles). The solid lines represent the estimated heat flow based on two different velocity–porosity relationships, the higher values being calculated by using the results from Erickson and Jarrard (1998) and the lower ones from Davis and Villinger (1992).

shot spacing). Examples of the seismic data are given in Fig. 9a–d.

Some prominent features generally associated with the occurrence of a BSR can be observed: (1) low reflectivity above the BSR in a few places, (2) enhanced reflectivity just below the BSR, and (3) a reflection amplitude of inverse polarity at the BSR, cutting through stratigraphic layering. In most parts of the profile seismic stratigraphy experiences only slight amplitude variation when interfering with the BSR. On the Makran accretionary complex strong seismic reflectors cut the BSR almost unchanged and weak reflectors often appear enhanced. As reported by Holbrook et al. (1996) low reflectivity above the BSR at the Blake Ridge is due to homogenous stratigraphy rather than velocity increase. The Makran data support the idea that increase of reflectivity due to free gas below the gas hydrate stability zone dominates by far the decrease of reflectivity due to gas hydrate cementing. In cases where the BSR cuts stratigraphy at an intermediate angle it appears as a variation of reflection amplitude rather than a horizon itself. Depth to BSR can be determined within an error of ± 5 ms with TWT times increasing from

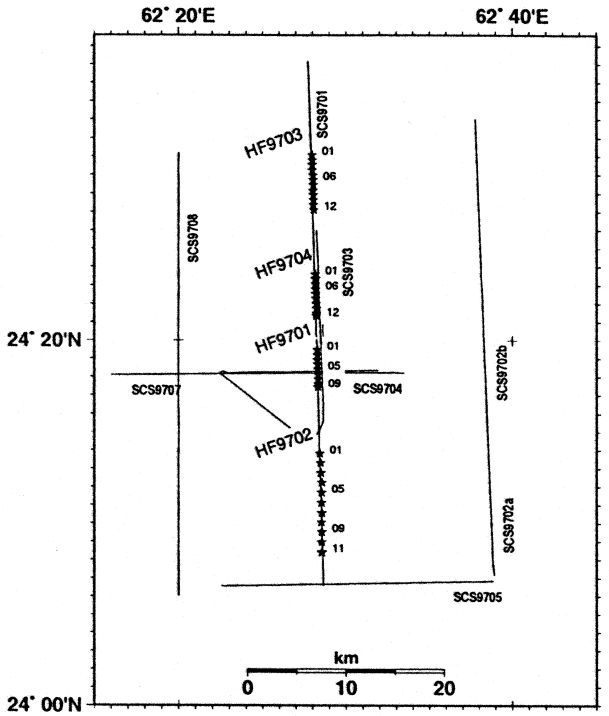

Fig. 3. Location map of heat flow stations along the central north–south trending seismic profile SCS9701.

about 0.62 s at 1850 m to about 0.75 s at 3200 m water depth. Interval velocity information cannot be deduced from single channel seismic data. Therefore, we rely on refraction seismic measurements (Fowler et al., 1985; Grevemeyer et al., 2000) and multichannel seismic data (Minshull et al., 1992; Fruehn et al., 1997). Velocity information from seafloor to the BSR is obtained at two locations (Fig. 3) from large aperture seismic profiles using ocean bottom hydrophones (OBH) parallel to strike (Grevemeyer et al., 2000). Results from these measurements are used in Section 4 to calculate the temperature field in the region above the BSR. Locations (OBH 4 + 6) were situated in the abyssal plain and in intermediate water depth in a syncline. Interpretation of refraction results gives a simple velocity structure with:

$$v_p(z) = 1500 + 3.451 \times z, \qquad 0 \le z \le 100, \qquad (1)$$

$$v_p(z) = 1845.1 + 0.783 \times z, \qquad 100 < z \le 1000 \qquad (2)$$

which represent the general increase of velocity v_p with depth z below seafloor. These functions are used to calculate the depth and temperature field above the BSR. The results of Grevemeyer et al. (2000) agree very well with data obtained from sonobuoy measurements (Fowler et al., 1985) and the velocity analysis of multichannel data, published by Fruehn et al. (1997).

3.2. Heat flow measurements

In this paper we report 42 new heat flow measurements across the accretionary wedge of the Makran subduction zone. Most of the heat flow sites were located in slope basins along a north–south oriented seismic profile (SCS9701) from south of the deformation front (water depth 3275 m) to a water depth of about 2050 m. Fig. 3 shows the location of the four heat flow stations on the central seismicline (SCS9701). The stations comprise a number of 47 penetrations from which 42 gave reliable heat flow values.

All measurements were made with a violin-bow type heat probe of 3.5 m length (Hyndman et al.,

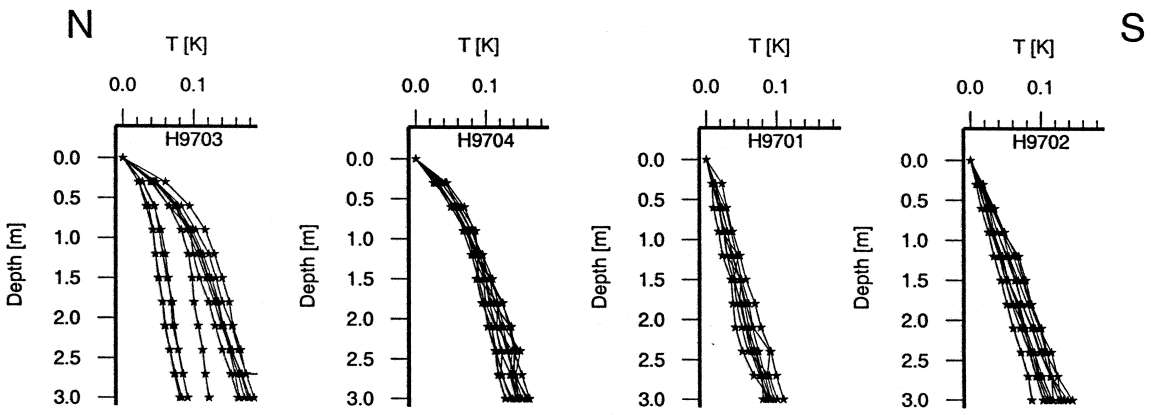

Fig. 4. Temperature profiles of 42 measurements. Temperatures are relative to seafloor temperatures and plotted against penetration depth. The order of stations from left to right reflect the increasing water depth of 2200, 2360, 2490 and 3100 m, respectively. The upper 1–1.5 m of shallow stations show temperature disturbances. Heat flow can be determined from the lower undisturbed part.

1979), which is based on an original design of Lister. Resolution of relative temperature measurements is better than 2 mK. In situ conductivity measurements according to the method of Lister (1979) were done at every other site. Undisturbed sediment temperatures and thermal conductivities are derived from the temperature decays by the method of Villinger and Davis (1987).

The instrument was deployed on a coax wire from the ship, allowing data transmission and operation control in real time. Surficial seafloor sediments appeared to be soft and allowed full penetration at all sites up to the uppermost sensor. Positioning of the vessel during heat flow stations was maintained using differential GPS all the time. Therefore a distance of 0.5 or 1 km between penetrations could be realized trying to minimize undersampling of local variations in heat flow. The lag of the instrument behind the ship (typically 100–200 m) was monitored at all times using a shipboard Ultra Short Baseline array (USBL). In general the accuracy of the probe's position on site is better than 50 m.

The results are shown in Fig. 4. It is obvious that transient temperature disturbances in the upper 1.5 m of sediment become more pronounced with decreasing water depth. These disturbances can be explained by a recent change in bottom water temperature. Gradients below approx. 1.5 mbsf are constant and allow the calculation of the steady state heat flow. The scatter of gradients, especially at station H9703, reflects the variation of heat flow values, related to the topographic variation along the station H9703.

In situ measurements of thermal conductivity were successful at 21 penetrations. Fig. 5 shows all values with a mean regional value of 1.27 W/m K. This mean is slightly higher than the value of 1.2 W/m K, published by Hutchison et al. (1981) who measured the thermal conductivity with needle probes on sediment cores. They attribute this relatively high value for high porosity surficial sediments to the high quartz content. Apart from the upper 0.5 m there is no significant increase of thermal conductivity with depth indicating very little porosity decrease in the uppermost meters. This is consistent with the high sedimentation rate in this area.

All measurements are summarized in Table 1. No corrections for transient bottom water effects or sedimentation have been applied at this stage.

4. Heat flow estimates based on BSR depth

It is possible to calculate the geotherm (and the heat flow) above the BSR from the position of the BSR below seafloor, measured in seconds and a known velocity–depth function. The calculation assumes purely conductive heat transfer. First we estimate the temperature at the BSR using the stability curve of gas hydrates, then we derive a thermal conductivity–depth function using the velocity–depth

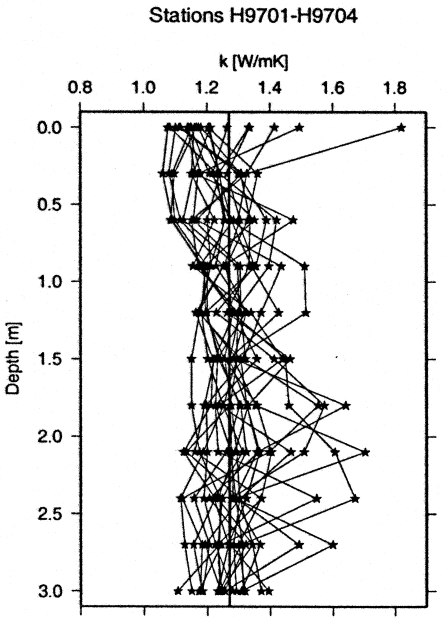

Fig. 5. Thermal conductivity measurements. Depth dependence of k is not significant, so it can reasonably be approximated by its mean value of 1.27 W/m K.

profile. The different steps necessary to calculate the geotherm (and heat flow at the seafloor) above the BSR are explicitly noted in Appendix A.

The temperature estimate at the depth of the BSR is based on the dissociation temperature–pressure function $T(p)$ published by Dickens and Quinby-Hunt (1994).

Heat flow estimates at BSR depth require the knowledge of a velocity–depth function $v_p(z)$ and thermal conductivity structure $k(z)$ (see Eq. (A2)). While $v_p(z)$ can be derived directly from refraction experiments (Grevemeyer et al., 2000), thermal conductivity at depth can only be inferred from empirical relationships describing the influence of porosity on v_p and relating thermal conductivity to porosity.

One way to estimate porosity at depth is to use published relationships of $v_p(\phi)$. In the following calculations we use two different but equally suited functions to demonstrate the crucial influence of porosity structure on calculated heat flow. The first one was published by Davis and Villinger (1992) and later used by Yuan et al. (1994) (see Eq. (A3)). It is based on the results from Cascadia ODP boreholes (ODP Leg 146) and is appropriate to use, as the tectonic setting is quite similar to the Makran accretionary prism.

The second relationship was published by Erickson and Jarrard (1998) (see Eq. (A4)) and probably gives the most complete overview on velocity and porosity relationships in marine environments. They incorporate a large number of investigations and results from ODP boreholes and measurements on cores as well as other previously published data in their analysis and distinguish also between different consolidation regimes. Their formula for normally consolidated sediments is rather complicated in order to take into account the consolidation.

The basic equation:

$$T(z) = T_0 + q \int_0^z \frac{dz'}{k(z')} \tag{3}$$

can now be used to calculate the heat flow after converting the two-way-travel time to the BSR into depth:

$$q = \frac{T_{BSR} - T_0}{\int_0^z dz'/k(z')} \tag{4}$$

It is obvious by inspecting Eq. (4) that the calculated heat flow depends on the integrated thermal resistance $1/k(z)$ with $k(z)$ as a function of porosity and hence on velocity structure.

Fig. 6 displays the basic steps of the calculation procedure: the velocity–depth function (Fig. 6a) is converted to a porosity–depth function. Thermal conductivity, calculated as the geometric mean of a binary system of seawater ($k_f = 0.6$ W/m K) and matrix conductivity ($k_m = 3.9$ W/m K) is shown in Fig. 6c. Integrating the inverse thermal conductivity gives the thermal resistance $R(z)$ (Fig. 6d). The seismic observations measured in s TWT have to be converted to depth using the velocity–depth relationship (Fig. 6e). All sediment physical properties depending on porosity are calculated with both relations discussed above. Fig. 6 shows very clearly that the Davis–Villinger relationship results in higher porosities than Erickson–Jarrard which leads to lower thermal conductivities. The effect of this difference on heat flow calculations based on BSR-depth will be discussed later.

Eqs. (1), (A2)–(A4) describe the sediment physical

Table 1
Heat flow results

Station name	Pen no.	Longitude E (deg:min)	Latitude N (deg:min)	Water depth (m)	Heat flow (mW/m^2)	Thermal conductivity (W/m K)	Seismic profile shot no.
H9701	1	62:28.2179	24:19.5402	2488	43	1.24	1162
H9701	2	62:28.3072	24:19.1971	2493	33	na	1183
H9701	3	62:28.2939	24:18.9202	2492	38	1.26	1202
H9701	4	62:28.3131	24:18.6912	2492	34	na	1220
H9701	5	62:28.3173	24:18.4153	2492	36	1.25	1241
H9701	6	62:28.3237	24:18.1329	2493	38	na	1262
H9701	7	62:28.3328	24:17.8766	2489	43	1.24	1281
H9701	8	62:28.3452	24:17.6113	2487	38	na	1301
H9701	9	62:28.3525	24:17.4449	2479	38	1.25	1312
H9702	1	62:28.4301	24:13.8238	3143	55	1.26	1580
H9702	2	62:28.4690	24:13.2956	3146	41	na	1618
H9702	3	62:28.4990	24:12.7532	3130	60	1.25	1659
H9702	4	62:28.5372	24:12.2147	3099	46	na	1698
H9702	5	62:28.5487	24:11.6709	3058	47	1.23	1738
H9702	6	62:28.5290	24:11.1222	3031	42	na	1779
H9702	7	62:28.5377	24:10.5724	3047	35	1.19	1820
H9702	8	62:28.5260	24:10.0412	3112	50	na	1859
H9702	9	62:28.5738	24:9.5221	3227	na	na	1898
H9702	10	62:28.5615	24:8.9748	3258	42	na	1938
H9702	11	62:28.5532	24:8.4254	3273	48	1.3	1979
H9702	12	62:28.5567	24:8.3979	3275	46	1.3	1981
H9703	1	62:27.9767	24:30.0714	2148	34	1.23	379
H9703	2	62:28.0110	24:29.7943	2206	47	na	399
H9703	3	62:27.9955	24:29.5415	2215	44	1.21	418
H9703	4	62:28.0122	24:29.2675	2214	42	na	438
H9703	5	62:28.0511	24:28.9880	2207	37	1.2	459
H9703	6	62:28.0476	24:28.7401	2195	45	na	478
H9703	7	62:28.0570	24:28.4651	2132	na	na	498
H9703	8	62:28.0428	24:28.1583	2051	24	na	521
H9703	9	62:28.0568	24:27.9198	2039	32	1.25	539
H9703	10	62:28.0760	24:27.6405	2045	24	na	558
H9703	11	62:28.0128	24:27.3696	1973	na	na	578
H9703	12	62:28.0948	24:27.1012	2179	na	na	598
H9704	1	62:28.1715	24:23.6053	2371	36	1.36	857
H9704	2	62:28.2021	24:23.3885	2372	38	na	874
H9704	3	62:28.1802	24:23.3623	2370	na	na	876
H9704	4	62:28.1953	24:23.0692	2370	32	1.36	897
H9704	5	62:28.1852	24:23.0666	2371	36	1.38	897
H9704	6	62:28.1866	24:22.7787	2369	49	na	918
H9704	7	62:28.2044	24:22.5368	2367	43	1.38	936
H9704	8	62:28.2069	24:22.2797	2363	39	na	955
H9704	9	62:28.2294	24:21.9901	2357	40	1.3	977
H9704	10	62:28.2479	24:21.7390	2350	40	na	996
H9704	11	62:28.2433	24:21.4620	2332	30	1.26	1016
H9704	12	62:28.2294	24:21.3408	2309	38	na	1025

properties in the subsurface primarily on the basis of the velocity–depth profile. However there is an inconsistency between the predicted and the measured thermal conductivity in the uppermost 10–20 m of the sediment. A porosity of about 75%, a result of using Eq. (A3), gives a surface thermal conductivity of about 1 W/m K (after Eq. (A2)) with a relatively high matrix thermal conductivity of 3.9 W/m K. The

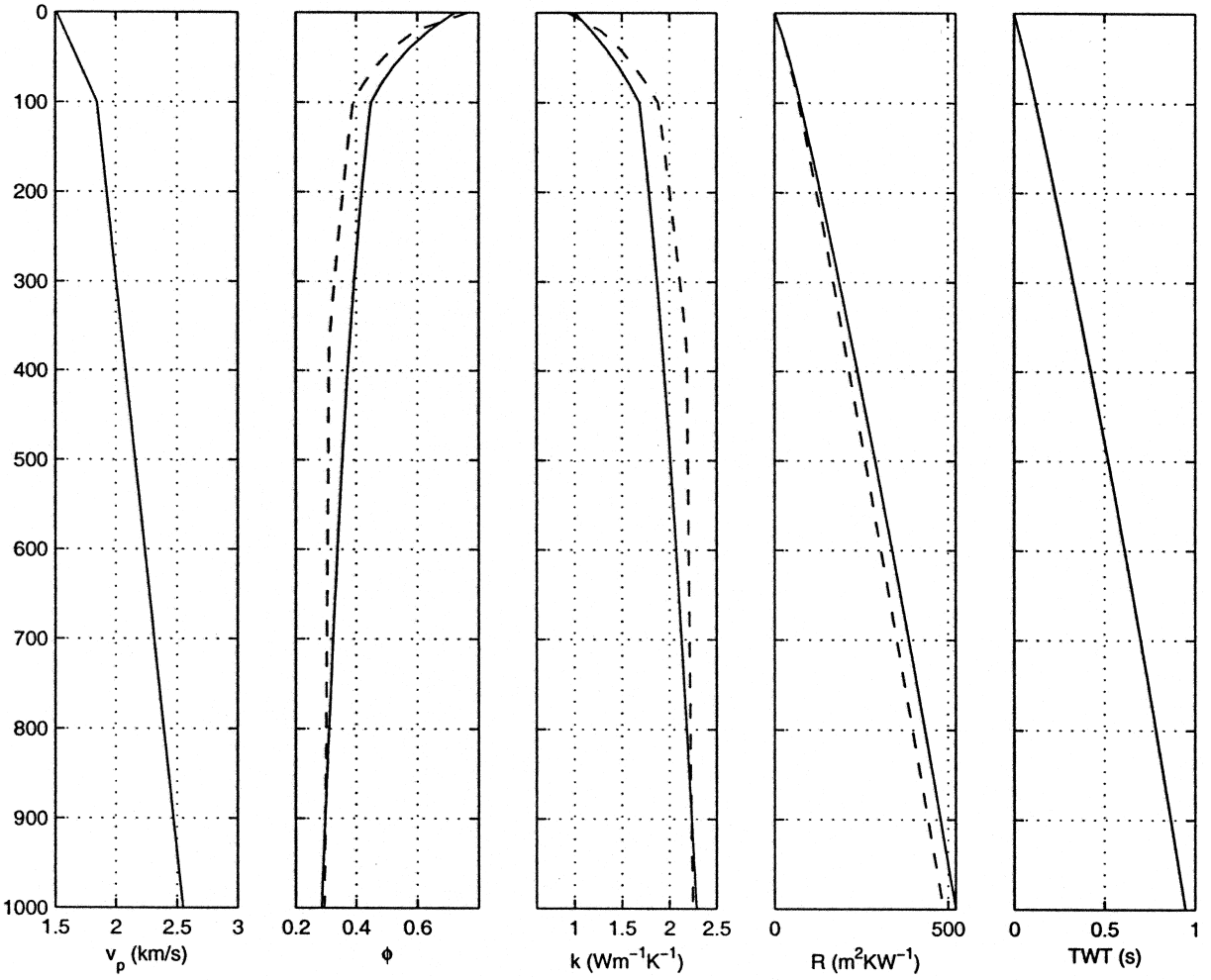

Fig. 6. Calculated physical properties based on velocity–depth functions and velocity–porosity relationships: (a) velocity vs. depth as derived by Grevemeyer et al. (2000) and described in Eq. (1); (b) porosity vs. depth based on Davis and Villinger (1997) (solid line) and Erickson and Jarrard (1998) (dashed line); (c) thermal conductivity vs. depth calculated as the geometrical mean of a binary system of seawater k_f = 0.6 W/m K and sediment matrix k_m = 3.9 W/m K after Brigaud and Vasseur (1989); (d) integrated thermal resistance, based on results from (c); (e) two-way-travel time vs. depth.

measured mean thermal conductivities—in situ (this study) and on cores as published by Hutchison et al. (1981)—are 1.27 and 1.2 W/m K, respectively. This inconsistency cannot be resolved for high porosity sediments as the seismic velocity in contrary to thermal conductivity is almost independent of porosity if $\phi > 75\%$. However this underestimation of thermal conductivity has very few consequences for calculation of the temperature at BSR-depth.

The error of estimated heat flow at the seafloor is difficult to assess as the calculation procedure makes error propagation not easy to analyze. In addition all errors related to the velocity–depth and velocity–porosity relationships are only quantifiable in error bounds of about $\pm 10\%$. Therefore we assume that the errors of the calculated heat flow values, based on BSR depth, are in a range of $\pm 10\%$.

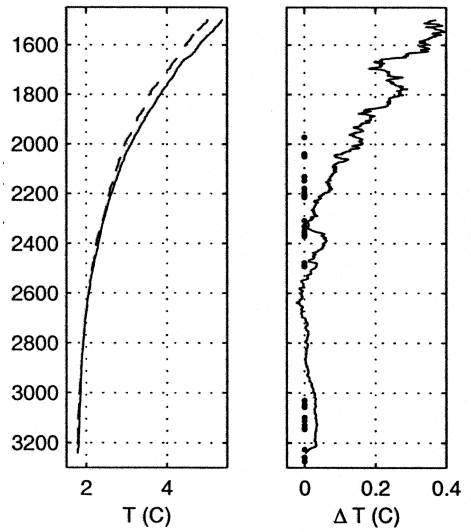

Fig. 7. Comparison of CTD casts. Two CTD profiles were measured at the same location within 4 weeks. The plot on the left shows the temperature structure of the water column, measured during SO123, the plot on the right shows the temperature differences between the measurements during SO124 and SO123 ($T_{SO124} - T_{SO123}$). The amplitude of the temperature difference decreases substantially with depth but a signal is still visible below 3000 m. Dots in the right plot indicate water depth where heat flow measurements were made.

5. Discussion

5.1. Transient temperature effects in the sediment

The occurrence of bottom water temperature fluctuations, indicated by disturbed temperature gradients of sediment layers of Station H9703 and H9704 is a well-known phenomenon. This effect often occurs in heat flow measurements in shallow water. If one compares two CTD profiles (Sea-Bird instrument SBE-9) made about one month apart during SO123 and SO124 (Flueh et al., 1997; Villinger and Scientific Party SO124, 1997) it becomes obvious that temperature of the complete water column is changing rapidly with time. Both CTD casts were located almost at the same location south of the deformation front in a water depth of 3270 m. Fig. 7a shows one temperature profile (October 8, 1997) and temperature differences (Fig. 7b). The most likely explanation is an increased upwelling of cold deep water during the summer. The maximum amplitude of the temperature difference of 1°C between 700 and 900 m water depth decreases substantially with increasing depth and vanishes in the deepest part of the profile.

5.2. Crustal age and sedimentation correction

Hutchison et al.'s (1981) age estimate was based on the Parsons and Sclater cooling model of the oceanic crust (Parsons and Sclater, 1977) which was refined by Stein and Stein (1994) by using a larger heat flow data set and by jointly inverting heat flow and basement depth. After Stein and Stein (1994), heat flow as a function of crustal age is given by:

$$q(t) = \frac{510}{\sqrt{(t)}}, \qquad t \leq 55 \text{ Ma}, \tag{5}$$

$$q(t) = 48 + 96\, e^{-0.0278t}, \qquad t > 55 \text{ Ma} \tag{6}$$

with time t in millions of years and the result in mW/m^2. In the case of the estimated age span of the Makran accretionary prism (70–100 Ma), the undisturbed heat flow from Eq. (5) would be 62 and 54 mW/m^2, respectively. The considerably lower measured values of either 42 mW/m^2 (Hutchison et al., 1981) or 47 mW/m^2 (this study) reflect the influence of rapid sedimentation. Assuming a mean age of the prism of 85 Ma as suggested in Hutchison et al. (1981) one obtains a model heat flow of 57 mW/m^2. This results in a necessary correction of 18% to be consistent with measured heat flow of 47 mW/m^2. A correction of 18% is considerably less than the value of 35% used by Hutchison et al. (1981) but still reasonable.

In a more detailed analysis, Hutchison (1985) includes compaction in the calculation of sedimentation on heat flow. His recalculation for the Gulf of Oman results in a correction of 10–20% which is half of his earlier estimate. This range of lower correction values agrees well with an estimate based on crustal age, and also with a calculated sedimentation correction at a sedimentation rate of 0.25 mm/a (Prins et al., 1999), for a duration of about 40 Ma. (see Fig. 8)

5.3. Discussion of heat flow

As an overall trend it can be observed that the

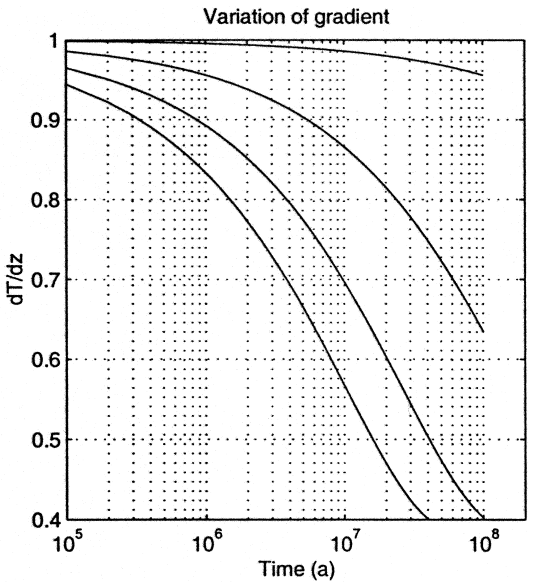

Fig. 8. Effect of high sedimentation rates on the thermal gradient. Horizontal axis represents duration of sedimentation in years, the vertical axis denotes the relative reduction of gradient. Four graphs indicate different sedimentation rates (from left to right: 0.4, 0.25, 0.1, 0.01 mm/a (adopted from von Herzen and Uyeda, 1963). Sedimentation rates greater than 0.25 mm/a as common on the Makran continental margin yield a disturbance of up to 50% after more than 30 Ma.

measured heat flow values as well as calculated values from BSR depth show a small decrease from the deformation front landward towards the accretionary wedge (Fig. 2). This trend is familiar from other accretionary prisms and related to the thickening of the sedimentary sequence as described by Wang et al. (1993). The slight increase of BSR-derived heat flow at the margins of the sediment basins are most likely caused by a change in the velocity structure within the deformed ridges causing changes in depth and therefore temperature at the BSR. These lateral variations are not accounted for in the constant velocity–depth model used for the lower part of the prism (see Grevemeyer et al., 2000) due to lack of data to resolve these variations.

It is observed that measured heat flow is significantly lower than the BSR-derived heat flow even if a 20% increase is added due to the large sedimentation rate. The sedimentation leads to a cooling of the subsurface and therefore shifts the stability zone to greater depth as the pressure (water depth) remains the same. This process is accompanied by a release of heat due to the exothermal nature of gas hydrate formation. However quantifying these competing processes is very difficult as the dynamic behavior of the complete system (gas hydrates, BSR formation) is currently not well known.

Fig. 9a–d displays the seismic profiles in detail at the heat flow sites together with measured and BSR-derived heat flow values. All profiles within the sedimentary basins (H9701, H9704 and H9703) lack strong systematic variations related to position within the basin i.e. a distinctive change at the northern or southern edges of the basins. Only the values on top of a deformation ridge (Fig. 9c, shotpoints 520–560) are significantly lower than the values in the adjacent basin. Values south of the deformation front (Fig. 9b) are about 10% higher than those published by Hutchison et al. (1981).

5.4. Discussion of observed versus estimated heatflow

The comparison of measured heat flow and BSR derived heat flow estimates points out two major features (a) a decrease of heat flow with increasing thickness of sediment pile when moving coastward and (b) a significant difference between both heat flow values. The effect of decreasing heat flow was already described by Ferguson and Westbrook (1993) and modeled by Wang et al. (1993). It is due to the subsidence of huge amounts of water within pore space that carries a low of thermal energy with it. Wang et al. (1993) point out that convective heat transport in an upward direction due to fluid expulsion is at least one order of magnitude smaller than the downward oriented effect of subsiding colder material. It appears that we see exactly this effect as increased heat flow cannot be observed, neither in the general picture nor locally where faults might be met. For an investigation of convection along fault lines, a station separation of 0.5 km might not be suitable and still suffers from undersampling. The discrepancy of heat flow measured at the seafloor level and those derived from 700 mbsl BSR yields a temperature difference of 5–6°C at the depth of BSR. Extrapolating the seafloor temperature into depth according to discussed conductivity–depth functions, we come up with a temperature too low at depth of BSR. A similar observation is described by Ruppel (1997) at

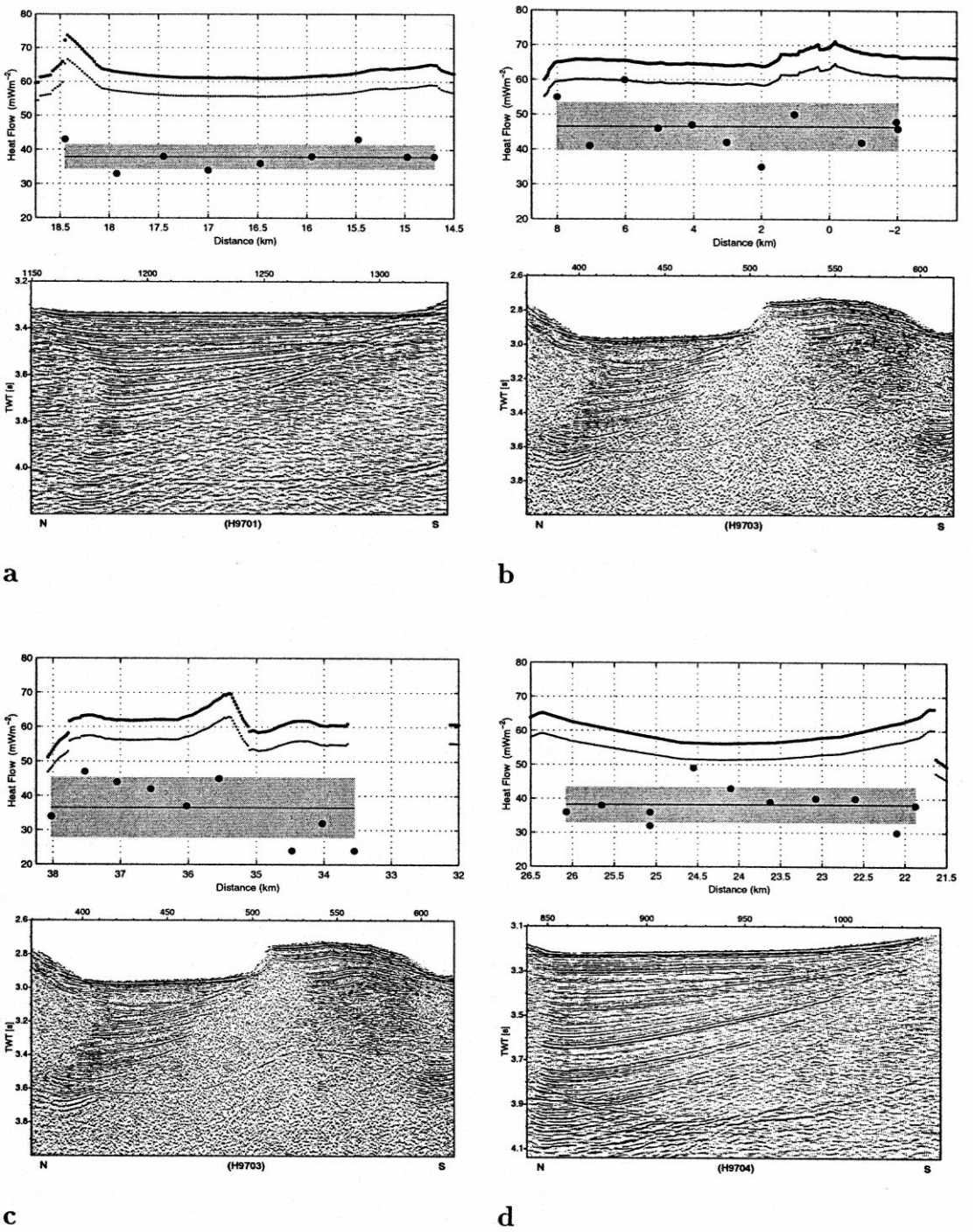

Fig. 9. Heat flow stations H9701–H9704: (a) upper left: station H9701; (b) upper right: station H9702, located near the deformation front; (c) lower left: station H9703, most coastward located station; and (d) lower right: station H9704, second most coastward station. Top part of ensembles: estimated heat flow for two porosity models (solid and dashed lines) and measured heat flow (solid circles) together with mean and standard deviation. Bottom part: time migrated seismic section.

the US continental margin. We calculated different conductivity–depth models with almost the same result: BSR-derived heat flow estimates are higher than measured. Or in reverse argumentation, measured heat flow yields lower temperatures at depth. Several assumptions had to be made for the physical properties of the interval between the BSR and seafloor. If we assume the *T–P* conditions according to Quinby-Hunt are applicable, as supported by ODP results and in-situ experiments of Brewer et al. (1997) then we have to look at the sediment section above the BSR. For finding the pressure condition at the BSR, we used hydrostatic pressure. This should be reasonable down to 2000 mbsl. Assuming lithostatic pressure would lead to the second end member for pressure consideration. This would yield results closer to measured values but less reasonable. Thermal conductivity is calculated by applying a two component system of water and matrix. In fact gas hydrate has to be considered as a third component which might modify the systems thermal conductivity considerably. Tzirita (1992) has shown that pure gas hydrates have thermal conductivities as low as 0.18–0.48 W/m K. Taking both effects of gas hydrates into account, increasing seismic velocity and decreasing thermal conductivity, a refined measurement of both effects might lead to a closer estimate of gas hydrate concentration in pore space. Discussion of different effects on temperature condition for hydrate stability by Ruppel (1997) points to the capillary forces in fine-grained materials. Investigations by Melnikov and Nesterov (1996) indicate that capillary inhibition may depress the dissociation temperature by 0.5–4°C or even 8°C.

An effect due to high sedimentation rate and tectonic uplift is the upward migration of gas hydrate stability conditions. Both effects lead to dissolution of gas hydrates at the base of GHSZ. Little is known about time constants of dissolution and gas hydrate generation. Thus it might well be that the base of the GHSZ is not in thermal equilibrium.

Important questions like the magnitude of the advective component of dewatering cannot be answered with the data available. In addition details about the nature of the BSR as discussed from a theoretical point of view by Xu and Ruppel (1999) will be extremely difficult to verify without drilling.

Acknowledgements

The authors would like to thank Captain Andresen, and the officers and crew of RV *Sonne*, who provided excellent ship handling and support during SO124. We thank Earl Davis and Ingo Pecher for reviewing the manuscript and substantial comments. Nina Kukowski kindly supplied a recent compilation of bathymetry data for Fig. 1. This research was funded by the German Federal Ministry of Education and Research, grant AZ BEO 03G0 124 A. We thank the Islamic Republic of Pakistan for research permission, namely Captain C.D. Bhatti and Z.M. Kahn.

Appendix A

The steps for calculating heat flow from an identified BSR using a depth-dependent thermal conductivity function can be summarized as follows:

1. In a purely conductive, one-dimensional regime the temperature $T(z)$ can be described by

$$T(z) = T_0 + q \int_0^z \frac{\mathrm{d}z'}{k(z')} \tag{A1}$$

   with z as depth, T_0 as the temperature at the seafloor $z = 0$, q as heat flow and $k(z)$ as vertical thermal conductivity profile. T_0 and q are known from measurements.
2. The thermal conductivity $k(z)$ is related to the porosity–depth profile by an empirical relationship of Brigaud and Vasseur (1989):

$$k(z) = k_{\mathrm{f}}^{\phi(z)} \times k_{\mathrm{m}}^{1-\phi(z)} \tag{A2}$$

   where $\phi(z)$ is the fractional porosity, k_{f} denotes thermal conductivity of the pore filling fluid and k_{m} of the matrix, respectively.
3. The increase of porosity with depth is related to an increase in seismic velocity. Two models for empirical velocity–porosity functions which are used in this investigation are described below. The first velocity–porosity relation after Davis and Villinger (1992) is:

$$\phi(v_p) = -1.18 + \frac{8.607}{v_p} - \frac{17.894}{v_p^2} + \frac{13.941}{v_p^3} \tag{A3}$$

where v_p is the interval velocity in km/s and ϕ the fractional porosity. Eq. (A3) is only valid for $\phi <$ 75% where the relationship reaches a value of $v_p =$ 1500 m/s. The second relationship was published by Erickson and Jarrard (1998):

$$v_p(\phi) = 0.739 + 0.552\phi + \frac{0.305}{(\phi + 0.13)^2 + 0.0725} + 0.61(v_{sh} - 1.123)[\tanh(40(\phi - 0.39)) - |\tanh(40(\phi - 0.39))|] \quad \text{(A4)}$$

with v_p as the compressional wave velocity of siliclastic marine sediments, ϕ as the fractional porosity and v_{sh} as the shale fraction. Because it is not possible to invert Eq. (A4), to calculate the porosity as a function of velocity a lookup table has been used.

4. The velocity–depth function in this investigation is determined from refraction seismic experiments and expressed as linear approximations:

$$v_p(z) = \begin{cases} 1500 + 3.451 \times z, & 0 \le z \le 100, \\ 1845.1 + 0.783 \times z, & 100 < z \le 1000. \end{cases} \quad \text{(A5)}$$

5. Temperature at the depth of the BSR T_{BSR} is calculated by using the dissociation temperature–pressure relation $T(p)$ (Dickens and Quinby-Hunt, 1994):

$$T(p) = \frac{1}{(3.79 \times 10^{-3} - 2.83 \times 10^{-4} \log p)} \quad \text{(A6)}$$

with p as the hydrostatic pressure in MPa, T in K and under the assumption of pure methane and seawater salinity of 35. Hydrostatic pressure—and depth—are calculated from converting the measured TWT at the BSR using a velocity–depth function. Finally the relationships described in Eqs. (A2)–(A6) can be used to calculate the heat flow:

$$q = \frac{T_{BSR} - T_0}{\int_0^z dz'/k(z')}. \quad \text{(A7)}$$

References

Brewer, P.G., et al., 1997. Deep-ocean field test of methane hydrate formation from a remotely operated vehicle. Geology 25 (5), 407–410.

Brigaud, F., Vasseur, G., 1989. Mineralogy, porosity and fluid control on thermal conductivity of sedimentary rocks. Geophys. J. 98, 525–542.

Davis, E.E., Villinger, H.W., 1992. Tectonic and thermal structure of the Middle Valley sedimented rift, northern Juan de Fuca Ridge. In: Davis, E.E., Mottl, M.J., Fisher, A.T. (Eds.). Proc. ODP, Initial Repts 139, College Station, TX Ocean Drilling Program.

Dickens, G.R., Quinby-Hunt, M.S., 1994. Methane hydrate stability in seawater. Geophys. Res. Lett. 21, 2115–2118.

Erickson, S.E., Jarrard, R.D., 1998. Velocity–porosity relationships for water-saturated siliclastic sediments. J. Geophys. Res. 103, 30 385–30 406.

Ferguson, L.J., Westbrook, 1993. Heat flow thermal models of the Barbados accretionary complex. J. Geophys. Res. 98 (B3), 4121–4142.

Flueh, E., Kukowski, N., Reichert, C., 1997. Fahrtbericht SO123, Mamut. 62, GEOMAR, Kiel.

Fowler, S.R., White, R.S., Louden, K.E., 1985. Sediment dewatering in the Makran accretionary prism. Earth Planet. Sci. Lett. 75, 427–438.

Fruehn, J., White, R.S., Minshull, T.A., 1997. Integral deformation and compaction of the Makran accretionary wedge. Terra Nova 9 (3), 101–104.

Grevemeyer, I., Rosenberger, A., Villinger, H., 2000. Natural gas hydrates on the continental slope off Pakistan: constraints from seismic techniques. Geophys. J. Int. 140, in press.

von Herzen, R.P., Uyeda, S., 1963. Heat flow through the eastern Pacific Ocean floor. J. Geophys. Res. 68, 4219–4250.

Holbrook, W.S., Hoskins, H., Wood, W.T., Stephen, R.A., Lizarralde, D., 1996. Leg 164 Science Party, methane hydrate and free gas on the Blake Ridge from vertical seismic profiling. Science 273, 1840–1843.

Hutchison, I., 1985. The effect of sedimentation and compaction on oceanic heat flow. Geophys. J. R. Astron. Soc. 82, 439–459.

Hutchison, I., Louden, K.E., White, R.S., 1981. Heat flow and age of the Gulf of Oman. Earth Planet. Sci. Lett. 56, 252–262.

Hyndman, R.D., Davis, E.E., Wright, J.A., 1979. The measurement of marine geothermal heat flow by a multipenetration probe with digital acoustic telemetry and in situ thermal conductivity. Mar. Geophys. Res. 4, 181–205.

Kukowski, N., Schillhorn, T., Flueh, E.R., Huhn, K., MAMUT Working Group, 1999. A newly identified strike-slip plate boundary in the northeastern Arabian Sea. Geology, submitted for publication.

Lister, C.R.B., 1979. The pulse-probe method of conductivity measurement. Geophys. J. R. Astron. Soc. 57, 451–461.

Melnikov, V., Nesterov, A., 1996. Modelling of gas hydrates formation in porous media. In: Proceedings, International Conference on Natural Gas Hydrates, 1996, pp. 541–548.

Minshull, T.A., White, R.S., 1989. Sediment compaction and fluid

migration in the Makran accretionary prism. J. Geophys. Res. 94 (B6), 7387–7402.

Minshull, T.A., White, R.S., Barton, P.J., Collier, J.S., 1992. Deformation at plate boundaries around the Gulf of Oman. Marine Geology 104, 265–277.

Parsons, B., Sclater, J.G., 1977. An analysis of the variation of ocean floor bathymetry and heat flow with age. J. Geophys. Res. 82, 803–827.

Prins, M.A., Postma, G., Weltje, G.J., 1999. Controls on late Pleistocene–Holocene sedimentation on the Makran continental slope. Geologica Ultraiectina 168, 145–172.

von Rad, U., 1999. MAKRAN II, Fahrtbericht, BGR, Hannover.

Roeser, H.A., Scientific Party SO122, 1999. MAKRAN I: the Makran accretionary wedge off Pakistan-tectonic evolution and fluid migration (part I). 116 643, BGR, Hannover.

Ruppel, C., 1997. Anomalously cold temperatures observed at the base of gas hydrate stability zone on the US passive continental margin. Geology 25 (8), 699–704.

Sloan, E.D., 1990. Clathrate Hydrates of Natural Gases, Marcel Dekker, New York, 641 pp.

Stein, C.A., Stein, S., 1994. Constraints on hydrothermal heat flux through the oceanic lithosphere from global heat flow. J. Geophys. Res. 99, 3081–3095.

Tzirita, A., 1992. In situ detection of natural gas hydrates using electrical and thermal properties. PhD Thesis, Texas A&M University, Offshore Technology Research Center, 220 pp.

Villinger, H., Davis, E.E., 1987. A new reduction algorithm for marine heat flow measurements. J. Geophys. Res. 92, 12 846–12 856.

Villinger, H., Scientific Party SO124, 1997. Fahrtbericht SO124, 4.10.—16.10.1997. 111 Fachbereich Geowissenschaften, Universitat Bremen, Bremen.

Wang, K., Hyndman, R.D., Davis, E.E., 1993. Thermal effects of sediment thickening and fluid expulsion in accretionary prisms: model and parameter analysis. J. Geophys. Res. 98 (B6), 9975–9984.

White, R.S., 1981. Deformation of the Makran accretionary sedimentary prism in the Gulf of Oman (north-west Indian ocean). In: Legett, J. (Ed.). Trench and Fore-Arc Sedimentation, Geological Society of London, London.

White, R.S., Klitgord, K., 1976. Sediment deformation and plate tectonics in the Gulf of Oman. Earth Planet. Sci. Lett. 32, 199–209.

White, R.S., Louden, K.E., 1982. The Makran continental margin: structure of a thickly sedimented convergent plate boundary. In: Watkins, J.S., Drake, C.L. (Eds.). Studies in Continental Margin Geology. Memoirs, American Association of Petrology and Geology, pp. 499–518.

Xu, W., Ruppel, C., 1999. Predicting the occurrence, distribution and evolution of methane gas hydrate in porous marine sediments. J. Geophys. Res. 104, 5081–5095.

Yamano, M., Uyeda, R.M., Aoki, Y., Shipley, T.H., 1982. Estimates of heat flow derived from gas hydrates. Geology 10, 339–343.

Yuan, T., Spence, G.D., Hyndman, R.D., 1994. Seismic velocities and inferred porosities in the accretionary wedge sediments at the Cascadia margin. J. Geophys. Res. 99, 4413–4427.